

See discussions, stats, and author profiles for this publication at: <https://www.researchgate.net/publication/230671888>

Hapticity Uncovered: Real-Space Bonding Indicators for Zincocene Chemistry

ARTICLE *in* CHEMISTRY - A EUROPEAN JOURNAL · SEPTEMBER 2012

Impact Factor: 5.73 · DOI: 10.1002/chem.201200870 · Source: PubMed

CITATIONS

16

READS

42

4 AUTHORS, INCLUDING:



Stefan Mebs

Freie Universität Berlin

54 PUBLICATIONS 516 CITATIONS

[SEE PROFILE](#)



Thomas Braun

Humboldt-Universität zu Berlin

120 PUBLICATIONS 2,851 CITATIONS

[SEE PROFILE](#)

Hapticity Uncovered: Real-Space Bonding Indicators for Zincocene Chemistry

Stefan Mebs,^{*,[a]} Maren A. Chilleck,^[a] Simon Grabowsky,^[b] and Thomas Braun^[a]

Abstract: The connectivities (hapticities) of asymmetric cyclopentadienyl zinc compounds are determined by theoretically obtained real-space bonding descriptors. The methods employed herein include the determination of the number of virial paths and electron localizability indicator (ELI-D) basins exhibited between the central Zn atom and the atoms of the ring system. Metal–ring interactions are characterized by flat electron densities and small density gradients, which are related to the high fluxionality of the rings. Due to this, the structures are topologically unstable and the conventional bond-path analysis within the atoms in molecules (AIM) scheme, which in principle can also be applied for experimental electron densities reconstructed from high-resolution X-ray diffraction data, is not a reliable tool for the determina-

tion of the hapticity. As a consequence, the theoretical investigation of other real-space bonding descriptors is the necessary primary step for discovering bonding modes that can be applied to molecular geometries obtained by subsequent experiments. By this procedure the common geometrical interpretation of connectivities, which is based on rather arbitrary decisions, is complemented by a self-consistent method using electronic descriptors. Moreover, the two-center σ contributions of all possible bonding scenarios (η^1 – η^5) were quantified by analyzing the electron populations of the Zn–C σ -bonding basins from the ELI-D analysis inside

Keywords: electron density • electron localizability • hapticity • cyclopentadienyl ligands • zincocenes

the AIM Zn atom in relation to the corresponding populations of the C–C π basins of the unsaturated rings. The investigation of the Zn–ring interactions is extended to the delocalization index, the source function, and a new type of electron-density-based surfaces, which we introduce here (ASF = aspherical stockholder fragments). They can be used for visualization of single atoms, fragments (e.g., functional groups), and whole molecules and are based on Hirshfeld's idea of stockholder partitioning, but apply aspherical electron densities. With these surfaces the charge accumulation between the chosen fragments and the steric accessibility of the central Zn atoms become visible, which is a useful tool for explaining and predicting chemical reactivity.

Introduction

Since the first synthesis of ferrocene in 1951,^[1] cyclopentadienyl complexes have played a key role in organometallic chemistry.^[2] Due to the large structural diversity,^[3] the un-

common (and often asymmetric) bonding patterns, the electronic properties,^[4] and the successful application as catalysts, for instance, in polymerization^[5] or hydroamination reactions,^[6] they have remained in focus of science until today. A major topic of discussion is the nature of the metal–carbocycle interaction. The discrimination between central and peripheral bonding of the metal atom to the ring system, denoted by η^5 and η^1 , respectively, is unambiguous. However, the discriminations between the different types of intermediate hapticities as well as the degree of σ and π bonding are not obvious. This can be seen in light of the structural fluctuations of these complexes: due to the flat potential energy surface of the rotation of the cyclopentadienyl ligands, X-ray diffraction analyses of solid-state structures tend to suffer from disorder of the rings. In solution, cyclopentadienyl zinc complexes are often highly dynamic, which in NMR experiments leads to averaged signals above the coalescence point. Thus, only one set of NMR signals can be found for all ten methyl groups in ZnCp^*_2 (Cp^* = pentamethylcyclopentadienyl).^[7] Likewise, theoretical calculations yield ab initio geometries of limited reliability. All these problems fortunately become less relevant with decreased molecular symmetries, which allows for a reliable classifica-

[a] Dr. S. Mebs, Dipl.-Chem. M. A. Chilleck, Prof. Dr. T. Braun
Department of Chemistry
Humboldt-Universität zu Berlin
Brook-Taylor-Str. 2, 12489 Berlin (Germany)
E-mail: stefan.mebs@chemie.hu-berlin.de

[b] Dr. S. Grabowsky
School of Chemistry and Biochemistry
Chemistry M313, The University of Western Australia
35 Stirling Highway, Crawley WA 6009 (Australia)

Supporting information for this article is available on the WWW under <http://dx.doi.org/10.1002/chem.201200870>. This includes structural superposition of the experimental structures of compounds **IV** and **V**; virial graphs of models **III**_{opt}, **IV**_{opt}, and **V**_{exp}; $d(\text{Zn}, \text{X})$ versus $\rho(r_{\text{bcp}})$, $G/\rho(r_{\text{bcp}})$, $H/\rho(r_{\text{bcp}})$, and $\delta(\text{Zn}, \text{X})$ for reference [25]; local source contributions for all Zn–C contacts in model **I**_{opt}; topological bond descriptors of the virial field for all models; ED mapped on the ASF surfaces of the ligands in models **II**_{exp}, **III**_{exp}, **IV**_{exp}, and **V**_{exp}; ELI-D representations of models **IV**_{opt} and **V**_{exp}; Cartesian coordinates of all models; important bond lengths, angles, and other geometrical parameters of all compounds; absolute source contributions of the Zn and C atoms to the Zn–C midpoints in models **I**_{opt} and **II**_{exp}.

tion of the Zn–Cp*–ring interactions based on real-space bonding indicators.

Cyclopentadienyl zinc complexes (like complexes of the heavier Group 12 metals) are much less intensively investigated in comparison with most other transition-metal cyclopentadienyl complexes. This is surprising because cyclopentadienyl zinc compounds exhibit an interesting structural diversity.^[3] The parent zincocene, ZnCp₂, is polymeric in the solid state. The bridging and terminal Cp ligands are reported to be η^1 or η^2 coordinated to the zinc atoms.^[3e] In contrast, decamethylzincocene, ZnCp*₂, exhibits a monomeric slipped-sandwich structure with each Zn atom bearing an η^5 - and an η^1 -coordinated Cp* ligand.^[3f] Based on DFT calculations and gas electron diffraction data, a similar slipped-sandwich structure was proposed to be adopted by ZnCp₂ in the gas phase.^[3g] The different types of hapticities attained by cyclopentadienyl complexes have been discussed among others by Jutzi and co-workers.^[8] In principle, the situation is comparable for complexes of any Cp-derived ligand, see Figure 1a. In the symmetric η^5 coordination mode the π

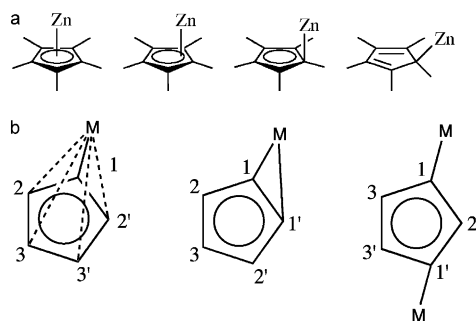


Figure 1. a) Zn–Cp* coordination schemes (from left to right): η^5 , η^3 , $\eta^1(\pi)$, and $\eta^1(\sigma)$; b) labeling scheme for odd-numbered Zn–C interactions (η^1 , η^3 , and η^5), even-numbered Zn–C interactions (η^2 , η^4), and two-times-bonded (see compound **I** below) Cp rings.

electrons of the Cp ring are completely delocalized. Intermediate hapticities, denoted by η^2 or η^3 , are caused by a significant shift of the Zn atom away from the position below the ring centroid (Cg, center of gravity); this leads to a more asymmetric bonding. Regarding η^1 coordination, two different cases have to be distinguished: $\eta^1(\pi)$ bonding is marked by a Cp_{Cg}–C1–Zn angle (Figure 1) close to 90° and coordination through the π electrons of the ring system whereas $\eta^1(\sigma)$ bonding is characterized by a peripheral localization of the Zn atom outside the ring perimeter.^[9] This goes along with a more sp³-hybridized C1 atom, the Cp_{Cg}–C1–Zn angle thus approaching the value of 109°, as well as alternating bond lengths in the Cp ring, corresponding to localized single and double bonds. The covalent amount of bonding is assumed to rise with decreasing hapticity, that is, from η^5 to $\eta^1(\sigma)$.

The labeling scheme used in this work is related to the hapticities (even or odd order type of connectivity) and the number of bonded Zn atoms, see Figure 1b.

In many experimental studies on cyclopentadienyl zinc compounds, the discussion about the hapticity is ambiguous.^[3e, 10–14] In several studies Zn–C bonds are assigned to Zn–C distances as long as approximately 2.5 Å. However, we think that the hapticity cannot be determined solely by consideration of the molecular geometries. Thus, in the present study, five asymmetric compounds are analyzed by the atoms in molecules (AIM)^[15] theory and the electron localization indicator (ELI-D):^[16] the cationic triple-decker complex [Zn₂Cp*₃]⁺ (**I**),^[14] the [ZnCp*(PN)]⁺ cation (**II**) (PN = Me₂N(CH₂)₂PiPr₂) as an example of a half-sandwich structure,^[14] the neutral compound ZnCp*^NCp*^N (**III**) (Cp*^N = C₅Me₄(CH₂)₂NMe₂),^[17] and the neutral complexes Zn{cyclo-MeC(BR)₂(NiPr)₂}₂ (R = Me (**IV**); R = Ph (**V**)) incorporating the Cp-analogue 1,2-diaza-3,5-diborolyl ligand.^[12] We will show that a distance-based criterion for hapticities can indeed be obtained by correlating to theoretically obtained real-space bonding descriptors and that the demarcation line for cyclopentadienyl zinc complexes is at about 2.3 Å.^[18] All analyzed contacts that are longer than that distance show neither a virial path in the AIM scheme nor an ELI-D basin between the Zn and the C atoms.^[19]

Quantum mechanically, transition-metal complexes are well examined.^[20] Since the early 1970s the metal–ligand bonding was also analyzed by density-based approaches,^[21] of course in a more qualitative fashion at that time. With the introduction of the AIM theory,^[15] a rigorous definition of the chemical bonding based on the electron density (ED) was available; this found wide applications as a complement for MO calculations, because the ED can in principle be obtained from theoretical calculations as well as from high-resolution X-ray diffraction data.^[22] By introduction of surfaces of zero electron flux (zfs), atomic basins and a corresponding bond-paths pattern are generated; this provides a straightforward interpretation scheme of atomic and bond properties. However, it turned out that the bond-path analysis, which unambiguously reflects the molecular structure for simple organic compounds, has some limitations for complex bonding scenarios, such as metal–metal bonds,^[23] borane cages,^[24] and metallocenes.^[25] Nowadays, new tools such as the source function (SF),^[26, 27] and the ELI-D are available; this promises deeper understanding of chemical interactions. The SF displays the amount of electron density provided by each atom to any reference point, that means, also for atoms that are not directly connected to the reference point. In such a way, delocalization effects can be manifested on absolute numbers. This is also possible with the delocalization index $\delta(A, B)$, introduced by Bader and Stephens.^[28, 29] The ELI-D is a further development of the electron localization function (ELF).^[30] Both concepts divide space into regions of localized electron pairs instead of atoms and therefore greatly complement the AIM theory. The partitioning follows the same rules that are used by AIM to separate atoms from each other. Thus, it is space filling and discrete, providing reliable integrated electron numbers of both core shells and (non)bonded valence electrons. Because of the orbital overlap, the obtained integrated electron numbers are

never equal to the expected integer values following from the Aufbau principle. Fortunately, the values in terms of ELF and ELI-D have been calculated for the free atoms^[31] so that the electron populations within the spherical core shells are known. The disadvantage of the ELF, not to be comparable between different molecules because the localization is related to a uniform electron gas of the very same compound, was discarded by the introduction of the ELI-D. Within this formalism, the absolute numbers can directly be compared between different compounds. Bonding basins between atoms X and Y are called disynaptic valence basins ($V_2(X,Y)$), unbound electron pairs and those that contain a proton (H atoms) are monosynaptic, because they are connected to one core only. The shape of the localization domain representations at specific ELI-D isovalues and the integrated amount of electrons within the ELI-D basins, as well as the topology (position and ELI-D value of the attractor), are useful indicators of the bond type. The topological similarities and differences between the Laplacian of the ED ($\nabla^2\rho(\mathbf{r})$) and the ELF were subject of an extensive theoretical study on several bond types.^[32]

In the last years, various attempts have been made to elucidate the bonding situation of cyclopentadienyl complexes by experimental electron density determination, see ref [25] and references therein. Because the electronic differences between the M–C bond critical points (bcp) and the ring critical points (rcp) of the C–M–C triangles turned out to be negligible, the lack of topological stability can be explained; this rules out the use of conventional bond-path analysis. Owing to these problems most studies could not reveal the correct hapticities. According to reference [25], the only reliable quantitative properties seem to be the integrated SF and the delocalization index: The former confirms that the cone-shaped region connecting the metal with the ring system gains charge from all atoms of the molecule. The latter seems to mirror the hapticity in an unambiguous way for less symmetric compounds. In 2004, Frison and Sevin published a theoretical study of the highly symmetric compounds ferrocene and bis(benzene)chromium by applying the ELF.^[33] They showed that all types of M–carbocycle interactions can be separated into M–C two-center (η^1) and C–M–C three-center (η^2) contributions. For both compounds, the η^1 and η^2 contributions were visualized and quantified by comparison of the electron populations of the M–C and C–C bonding basins. For ferrocene (bis(benzene)chromium) they found a relative contribution of 66 % (78 %) of the η^2 interaction, which the authors related to the pronounced aromaticities of the carbocycles. Herein we will show that this interpretation requires a modification for asymmetric metallocenes, because it is counterintuitive that the relative η^1 contributions should decrease with decreasing hapticity, which is a consequence of the method proposed by Frison and Sevin.

The visualization of single atoms, functional groups, and molecules in a crystal in terms of density-based surfaces helps to understand steric demands as well as electron distributions by mapping properties (e.g., the electrostatic po-

tential; ESP) on these surfaces. The most prominent surface types are the zfs boundaries within the AIM scheme, the 001 isosurface (the ED is cut at 0.001 au) and the Hirshfeld surface,^[34] which is defined by “stockholder partitioning”. In a variation of the latter, which uses spherically averaged electron densities of the different atom types, we use the aspherical densities of the individual atoms within their molecular environment and define the aspherical stockholder fragments (ASF) by the following weight function:

$$w_a(\mathbf{r}) = \rho_a^{\text{as}} / \sum_i \rho_i^{\text{as}}(\mathbf{r}); \text{ASF} \equiv w_a(\mathbf{r}) = 0.5$$

The aspherical atomic densities ρ_i^{as} are obtained from multipole refinements of theoretically obtained pseudoperiodic structure factors, but can in principle also be obtained from periodic calculations and experiments to get reliable shapes of molecules in crystals. Because the effects of intermolecular interactions are assumed to be negligible for the intramolecular electron distributions of the compounds investigated herein, periodic calculations were not applied.

Theoretical Calculations and Refinement Procedures

For compounds **I–IV** the molecular geometries were fully optimized at the BP86/TZVP^[35] level of theory with Gaussian03^[36] starting from the solid-state geometries obtained by routine X-ray diffraction. No imaginary frequencies were observed; this confirms all final geometries to be local minima. For comparison, calculations were also performed for the fixed experimental geometries of compounds **II–IV**. For compound **V**, which is larger than compounds **I–IV**, the wave function was calculated only for the experimental geometry at the same level of theory.

The wave functions were analyzed with a set of different programs to obtain all desired bonding descriptors: The ELI-D and some integrated AIM properties (charges and volumes) were calculated with DGRID-4.5^[37] by using a grid step size of 0.04 bohr. Virial paths were displayed and topologically analyzed with AIM2000.^[38] Nonclassical AIM derived properties, such as the delocalization index and the SF, were calculated with AIMALL.^[39] Finally, theoretical structure factors were generated with the program TONTO^[40] (pseudoperiodic calculations) by using the checkpoint files obtained by GAUSSIAN03. Subsequent aspherical-atom refinements were performed with XD2006^[41] for the synthetic data sets by applying appropriate local symmetries and chemical constraints. All non-hydrogen atoms were expanded to the hexadecapolar level, whereas for H atoms only bond-directed multipoles were refined up to the quadrupole level of expansion. Subsequent refinements of the expansion/contraction parameters led to final multipole models, which were analyzed in terms of the new ASF surfaces by mapping the ED on them. ASF surfaces and ELI-D isosurfaces are generated with MOLISO.^[42]

Results and Discussion

Geometries: Figure 2 displays the molecular structures for compounds **I–IV** as superpositions of experimental (dark grey) and optimized (light grey) geometries and the experimental geometry of compound **V**. The energy gain of the optimization is 2311.3 kJ mol^{−1} for **I**, 1096.9 kJ mol^{−1} for **II**, 1068.5 kJ mol^{−1} for **III**, and 1615.9 kJ mol^{−1} for **IV**. Although the convergence criteria were set to a very tight level in all

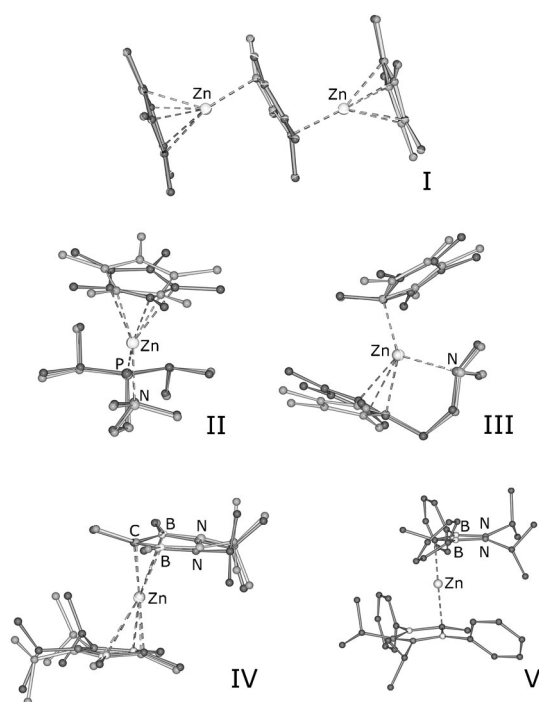


Figure 2. Experimental (dark grey) and optimized (light grey) structures of compounds **I–IV** and experimental structure of compound **V**. H atoms are omitted for clarity. SCHAKAL-representation.^[43]

cases, the final geometry of the triple-decker complex **I** remained slightly asymmetric and optically almost indistinguishable from the experimental structure. Due to this, only the optimized geometry of compound **I** is analyzed by means of electronic bond descriptors. In contrast, for compound **IV** only the experimental structure is analyzed in detail, because the overall structural changes are small as well and the experimental geometry is closer to an η^3 sce-

nario than the optimized geometry, which lies in the focus of our study. Large differences, however, are found for the experimental and optimized geometries of compounds **II** and **III**: Whereas the bidentate PN ligand remains unchanged in compound **II**, the asymmetrically oriented Cp^* fragment shows both a considerable rotation and a tilting. The former is in line with the fact that the experimental X-ray structure shows pronounced rotational disorder for Cp^* . After geometry optimization the plane of the Cp^* ligand is oriented almost parallel to the ligand's P–N axis nearly exhibiting mirror symmetry across the P–N–Zn plane. Thus, two C atoms approach the central Zn atom. Because these differences between experimental and calculated structures may indeed lead to different Zn–C connectivities, it is necessary to analyze the experimental and the optimized structures especially in the case of compound **II**. The observed tilting leads to larger Zn–C2 and Zn–C3 distances. A pronounced tilting is also found for the Cp^{*N} ligand in compound **III**, whereas the Cp^* ligand shows some rotation. For both compounds the tilting indicates larger sigma contributions in the Zn–C bonds of the optimized gas-phase structures as the Zn–C1–Cg angle becomes larger and the Cg–C1–Me angle deviates more from 180° .

In numbers (see Table 1 and for detailed lists the Supporting Information): All closest Zn–C contacts (Zn–C1) vary in the range of 2.00–2.19 Å and tend to lengthen with increasing hapticity. The slippage^[44] of the Zn atom along the (terminal) η^5 -bonded Cp^* rings in **I** is about 0.08 Å, whereas it is 1.34 Å (averaged) for the $\eta^1(\pi)$ -bonded Cp^* ligands (models: **I** Cp^*_{cen} (central Cp^* ring), **III**_{opt} Cp^{*N} , and **V**_{exp}), and about 1.78 Å for $\eta^1(\sigma)$ (compound **III** Cp^*). However, in the experimental geometries of compounds **II**, **III** (Cp^{*N}), and **IV**, the hapticities are not clear. They show slippage values of 0.55 Å (**II**), 0.80 Å (**III**), and 1.01 Å (**IV**). The location of the Zn atoms between a peripheral and a central

Table 1. Selected bond lengths [Å] and angles [°] of compounds **I–V** at experimental and optimized geometries and suggested hapticities derived from the geometrical parameters.

		$d(\text{Zn}–\text{C1})$	$d(\text{Zn}–\text{Cg})$	Slippage ^[44]	Zn–C1–Cg	Cg–C1–Me	Hapticity
I _{exp} ^[a]	Cp^*_{ter}	2.190	1.863	0.074	–	173.74	η^5
	Cp^*_{cen}	2.074	2.476	1.353	93.26	156.33	$\eta^1(\pi)$
I _{opt} ^[a]	Cp^*_{ter}	2.194	1.872	0.084	–	173.35	η^5
	Cp^*_{cen}	2.077	2.480	1.357	93.46	156.26	$\eta^1(\pi)$
II _{exp}	Cp^*	2.105	2.043	0.545	76.71 ^[b]	166.84	$\eta^3?$
	Cp^*	2.137	2.181	0.870	86.47 ^[b]	163.08	η^2
III _{exp}	Cp^{*N}	2.139	2.224	0.800	78.76	174.92	$\eta^3?$
	Cp^*	2.017	2.659	1.806	105.74	141.40	$\eta^1(\sigma)$
III _{opt}	Cp^{*N}	2.090	2.467	1.321	92.30	159.57	$\eta^1(\pi)$
	Cp^*	2.045	2.651	1.745	103.65	144.28	$\eta^1(\sigma)$
IV _{exp} ^[a]	CB_2N_2	2.002	2.271	1.008	84.32	162.46	$\eta^3?$
IV _{opt} ^[a]	CB_2N_2	2.036	2.383	1.170	88.06	160.44	$\eta^2?$
V _{exp} ^[a]	CB_2N_2	2.002	2.433	1.327	92.20	158.33	$\eta^1(\pi)$

[a] Two ring systems averaged; [b] angle between two planes: C1–Zn–C2 versus Cp^* ring plane. $\text{CB}_2\text{N}_2 = \text{MeC}(\text{BR})_2(\text{NiPr})_2$ (R = Me (**IV**), R = Ph (**V**)), $\text{Cp}^{*N} = \text{C}_5\text{Me}_4(\text{CH}_2)_2\text{NMe}_2$.

position points towards an η^2/η^3 type of bonding. However, the deviations of the Cg–C1–R (R=Me for **II** and **IV**, R=(CH₂)₂NMe₂ for **III**) angles from 180° (ca. 13° for **II**, ca. 5° for **III**, ca. 18° for **IV**) suggest partial sigma contributions. The results are supported by the C–C bond lengths alternation within the rings, see Figure 3 for an alternation pattern

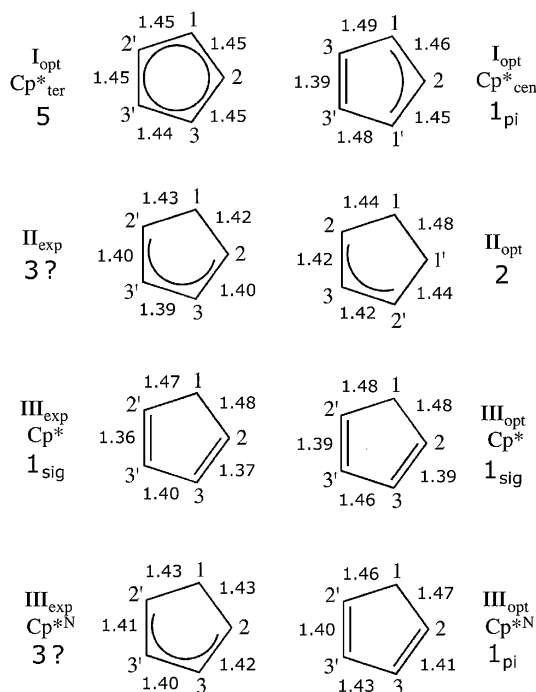


Figure 3. C–C bond lengths [Å] alternation within the rings of compounds **I–III**. The C–C bond lengths alternation is supposed to be related to the C–C bond delocalization. This is graphically represented following this rule: if the C–C bond opposite to the C1 atom (e.g., C3–C3') is longer than the two adjacent C–C bonds (e.g., C2(=)–C3(=)), it is drawn as single bond, independently of the absolute C–C bond distance. From these bonding schemes and the Zn–C distances, the possible hapticities are deduced.

for compounds **I–III**, so that a correlation between hapticity and C–C bond alternation within the rings can be assumed. For the diazadiborolyl heterocycles the C–B (B–N) bonds are longer (shorter) compared with the optimized gas-phase structures of the free ligands, but a clear classification of the hapticity by geometrical means is not possible.

Apparently, there is no geometrical parameter that unambiguously reveals the true bonding situation for models **II_{exp}**, **III_{exp}** Cp^{*N}, and **IV_{exp}**. The fact that only those rings for which the bonding situation is expected to be η^3 show a pronounced tilt away from the Zn atom in the process of geometry optimization in the gas phase suggests that this type of connectivity is mainly a consequence of the packing process within the crystalline environment. So we apply several real-space bonding descriptors for the determination of the hapticity and the quantification of the Zn–ring interaction in these asymmetric zincocene-related compounds.

Electron-density analysis: As mentioned in the introduction, the conventional bond-paths analysis within the AIM

scheme is not suitable to reliably characterize Zn–X (X=C, N, B) interactions in metallocene-related chemistry because of the low electron-density values and the flat density gradients between the metal atoms and the rings. As a consequence, the virial-paths pattern, which is based on the potential energy density field $V(r)$, is analyzed. The virial graphs are known to be less sensitive to the choice of the basis set and show all expected connections in an η^5 scenario; this is almost never the case for the bond-paths analysis even if they are derived from theoretical data.^[25] Figure 4 displays the virial graphs for models **I_{opt}**, **II_{exp}**, **II_{opt}**, **III_{exp}**, and **IV_{exp}**. The remaining depictions (**III_{opt}** and **V_{exp}**) are given in the Supporting Information. As expected, five (one) virial paths are exhibited between the Zn atom and the terminal (central) Cp^{*} ring in model **I_{opt}**, which confirms an η^5 (η^1) type of bonding, see Figure 4a. For models **II_{exp}**, **III_{exp}** (Cp^{*N}), and **IV_{exp}**, however, only one virial path is exhibited between the Zn atom and the ring, see Figure 4b,d, and e. According to the virial-paths analysis, η^3 bonding is not observed in any case. η^2 bonding is found for model **II_{opt}**, which thus follows the expectation from the geometrical analysis. Inspection of the molecular geometries shows that virial paths are found for all Zn–C contacts shorter than 2.28 Å with one exception: the Zn–C2 contact in model **II_{exp}** is 2.206 Å, but a virial path is not found. This is in accordance with the severe rotational disorder at the Cp^{*} ring of the crystalline structure of compound **II**.^[14] This leads to the possibility that the experimental structure is close to a catastrophe scenario, which is supported by the analysis of the ASFs and the ELI-D (see below). Our results compare well to the findings of Farrugia and co-workers, who found virial paths only for M–C contacts shorter than 2.3 Å.^[25] Assuming an η^2 -bonded Cp^{*} ligand as a two-electron donor, the complexes can be classified as 18 VE (VE = valence electrons) for **I**, approaching a linear coordination at the Zn atom, 16 VE for **II** and **III**, approaching a trigonal planar coordination at the Zn atom, and 14 VE for **IV** and **V**, approaching a linear coordination at the Zn atom.

The bond topological and integrated bond descriptors, as listed in Table 2, were extensively discussed by Farrugia et al.^[25] for other metallocene-related compounds and will thus only briefly be discussed here because our results are very much comparable to this earlier work. All Zn–C bonds show the typical characteristics of interactions between transition-metal and carbon atoms. On the one hand, the bonds are partially ionic, which is reflected in low $\rho(r_{\text{bcp}})$ values, the positive sign of the Laplacian, and the low electron sharing between Zn and C in terms of the delocalization index, $\delta(\text{Zn}, \text{C})$. The penetration of the C atom valence electrons into the outer core regions of the Zn atom leads to quite high kinetic density over rho ratios at the bcp ($G/\rho(r_{\text{bcp}})$). Covalent contributions on the other hand must not be neglected. The total energy density over rho ratio, $H/\rho(r_{\text{bcp}})$, is negative and the Laplacian, although being of positive sign, is still quite close to zero—two hints for covalent contributions. Due to the flat density gradients the bond ellipticities are quite large. As mentioned above, the electronic charac-

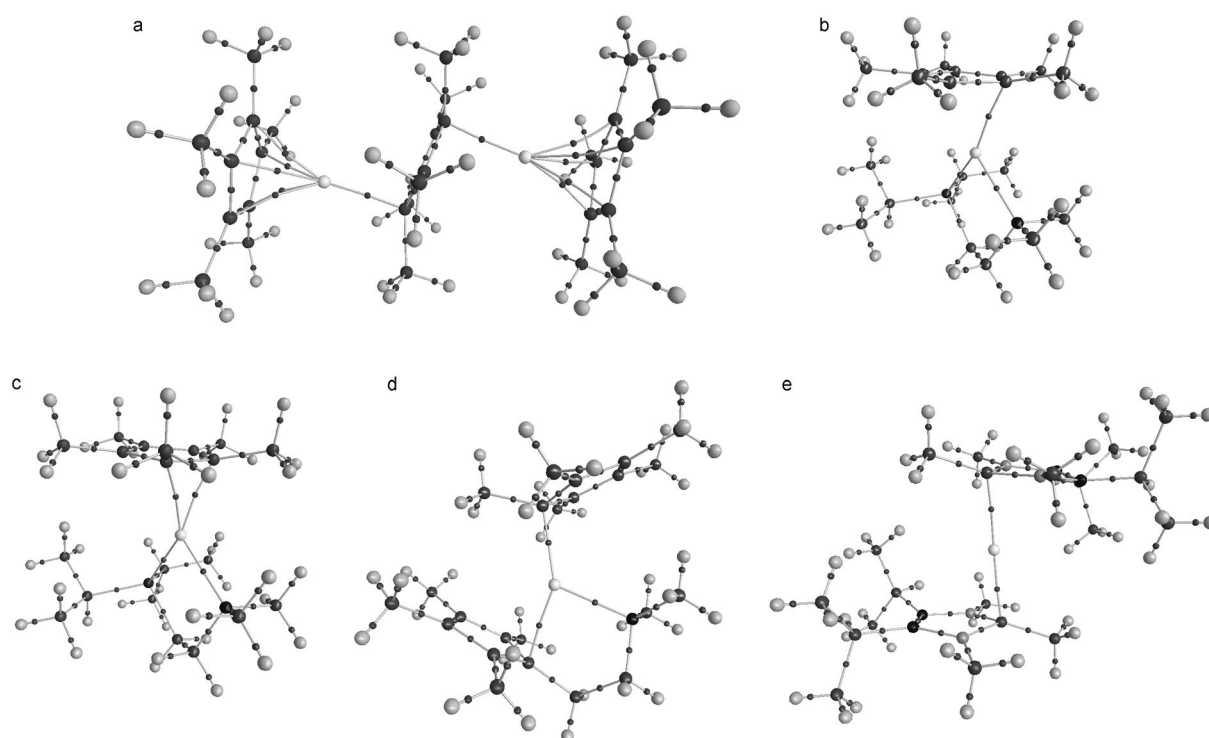


Figure 4. Virial graphs of models **I_{opt}** (a), **II_{exp}** (b), **II_{opt}** (c), **III_{exp}** (d), and **IV_{exp}** (e). Bcps are given as black dots. Bcps of weak intramolecular H···H contacts and ring and cage critical points are omitted for clarity.

teristics of the rcps, which were found in close proximity to the bcps, prove to be almost identical to the bcp values. This reflects the fact that already small perturbations of the molecular electron density may lead to a catastrophe scenario in which bond paths are generated or annihilated. The topological properties of the $V(r)$ field are in good accordance with those of the ED field, see the Supporting Information.

In ref [25] it was stated that the delocalization index and the SF are also useful and unambiguous discriminators of the hapticities. In contrast to that statement, we found pronounced dependencies of all AIM-derived bonding descriptors on the bond distances, see Figure 5 a–c. In Figure 5 a, $\rho(r_{\text{bcp}})$, $G/\rho(r_{\text{bcp}})$, and $H/\rho(r_{\text{bcp}})$ are plotted against the Zn–C, Zn–N, and Zn–P distances. Apparently, a linear relationship

Table 2. Topological and integrated AIM bond descriptors of the Zn–C bonds.^[a]

Model	Bond	$\rho(r_{\text{cp}})$ [eÅ ^{−3}]	$\nabla^2\rho(r_{\text{cp}})$ [eÅ ^{−5}]	d [Å]	d_1 [Å]	d_2 [Å]	ϵ	$G/\rho(r_{\text{cp}})$ [h e ^{−1}]	$H/\rho(r_{\text{cp}})$ [h e ^{−1}]	$\delta(\text{Zn,C})$	No.
I_{opt}	$\eta^1(\pi)$	0.48	4.2	2.077	1.022	1.055	0.10	0.82	−0.28	0.51	2
	η^5	0.36	4.4	2.220	1.074	1.151	4.37	0.92	−0.17	0.29	5
	rcp	0.36	4.5	–	1.078	1.252	–	0.92	−0.15	–	2
II_{exp} II_{opt}	$\eta^3?$	0.45	4.9	2.105	1.029	1.077	0.65	0.93	−0.24	0.37	1
	η^2	0.43	4.5	2.137	1.045	1.100	1.67	0.87	−0.22	0.40	2
	rcp	0.42	4.8	–	1.057	1.204	–	0.88	−0.17	–	1
III_{exp} (Cp*) III_{opt} (Cp*)	$\eta^1(\sigma)$	0.42	4.4	2.139	1.042	1.097	0.39	0.89	−0.23	0.32	1
	$\eta^1(\sigma)$	0.48	4.3	2.090	1.023	1.067	0.10	0.83	−0.27	0.46	1
III_{exp} (Cp* ^N) III_{opt} (Cp* ^N)	$\eta^3?$	0.56	4.6	2.017	0.994	1.023	0.02	0.84	−0.32	0.62	1
	$\eta^1(\pi)$	0.53	4.3	2.045	1.005	1.040	0.02	0.81	−0.30	0.60	1
IV_{exp} V_{exp}	$\eta^3?$	0.57	4.6	2.002	0.997	1.005	0.18	0.83	−0.33	0.73	1
	$\eta^1(\pi)$	0.58	4.3	1.999	0.997	1.002	0.09	0.81	−0.34	0.75	1

[a] Averaged AIM-derived bonding descriptors. For all bonds, $\rho(r_{\text{cp}})$ is the ED at the bcp or rcp; $\nabla^2\rho(r_{\text{cp}})$ is the corresponding Laplacian; $d = d_1 + d_2$, d_1 (d_2) is the distance of the Zn (C) atom to the bcp or rcp; ϵ is the bond ellipticity ($\epsilon = (\lambda_1/\lambda_2) - 1$; $\lambda_1 > \lambda_2$); $G/\rho(r_{\text{cp}})$ and $H/\rho(r_{\text{cp}})$ are the kinetic and total energy density over $\rho(r_{\text{cp}})$ ratios; $\delta(\text{Zn,C})$ is the delocalization index, no. is the number of averaged values.

is found for all three descriptors. Unexpectedly, $G/\rho(r_{\text{bcp}})$ shows a small increase with increasing Zn–C distances, whereas the Zn–N and Zn–P interactions show the expected decrease. In Figure 5 b the delocalization index, $\delta(\text{Zn,X})$ with X = B, C, N, P, is plotted against the atom–atom distances for all Zn–X pairs of the models **I_{opt}**, **II_{opt}**, **III_{opt}**, and **V_{exp}**. Almost all $\delta(\text{Zn,B})$, $\delta(\text{Zn,C})$, and $\delta(\text{Zn,N})$ values lie very close to the best-fit line. The only obvious exception of about 0.6 electron pairs at approximately 2.4 Å arises from the Zn–P contact in model **II_{opt}**. The results of Figure 5 a,b suggest that AIM-derived bonding descriptors are hardly able to

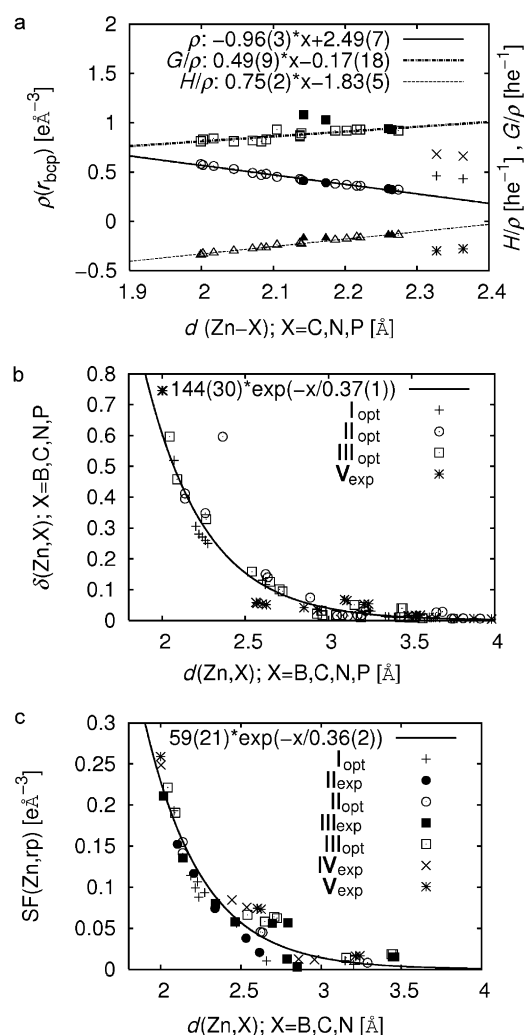


Figure 5. Dependency of topological (a) and integrated (b, c) AIM bond descriptors against the Zn–X ($X = \text{C, N, B, P}$) distances. a) $\rho(r_{\text{bcp}}) = \circ$ (Zn–C), \bullet (Zn–N), and $+$ (Zn–P); $G/\rho(r_{\text{bcp}}) = \square$ (Zn–C), \blacksquare (Zn–N), and \times (Zn–P); $H/\rho(r_{\text{bcp}}) = \triangle$ (Zn–C), \blacktriangle (Zn–N), and $*$ (Zn–P), all models are included. b) Analysis of delocalization index $\delta(\text{Zn}, X)$, $X = \text{non-H}$ atoms versus Zn–X distances, four models included. c) Analysis of the source contributions of the Zn atom in all Zn–X ($X = \text{C, N, B}$) midpoints, all models included.

discriminate between Zn–C and Zn–N bonds in this class of compounds. The Zn–P contacts, however, are clearly discriminated from Zn–C and Zn–N contacts. In Figure 5c the absolute source contribution of the Zn atom to the five Zn–C/B/N midpoints is plotted against the Zn–C/B/N distances, irrespectively if a bond path is exhibited or not. Again, there is a pronounced dependency between source contribution and Zn–C/B/N distance, but in the region between 2.4–2.8 \AA some deviations from the best-fit line are found; these may be assigned to intensified or reduced chemical interactions. However, the absolute values are very small due to the delocalized nature of the Zn–ring interaction, which limits the significance. The AIM results of earlier works show comparable trends, so that one may conclude that all quantitative AIM descriptors are suitable for the determina-

tion of the bond properties, but not for the hapticity, which by definition is a yes/no-based bonding criterion. Analysis of the local source contribution^[45] reveals that the density shared between Zn and C atoms is almost exclusively provided by the C atoms, see Figures 4 and 5 in the Supporting Information for details.

The electron density analysis will be completed by inspection of the atomic AIM charges that, added up for all atoms of the ligand, provide insight into the amount of charge transfer between the central Zn atom and the ligands, see Table 3. For the cationic compound **I**, the positive charge is

Table 3. AIM charges of the functional groups in all models.^[a]

model	Q_{tot} [e]	Ligand 1	Q_{tot} [e]	Ligand 2	Q_{tot} [e]	Σ [e]
for Zn						
I _{opt}	2.0.91	2 Cp* _{ter}	−0.32	Cp* _{cen}	−0.20	0.98
II _{exp}	0.86	Cp*	−0.36	PN	0.50	1.00
II _{opt}	0.83	Cp*	−0.31	PN	0.48	1.00
III _{exp}	0.91	Cp*	−0.45	Cp* ^N	−0.45	0.01
III _{opt}	0.88	Cp*	−0.45	Cp* ^N	−0.43	0.00
IV _{exp}	0.79	2 CB ₂ N ₂	−0.39	–	–	0.01
V _{exp}	0.78	2 CB ₂ N ₂	−0.39	–	–	0.00

[a] Q_{tot} are the total AIM charges, Σ is the sum of all total AIM charges within one model. The ligands are abbreviated as follows: PN = Me₂N-(CH₂)₂PiPr₂; CB₂N₂ = MeC(BR)₂(NiPr)₂ (R = Me (**IV**), R = Ph (**V**)).

located solely at the two Zn atoms. As expected, the central Cp* ring carries a smaller amount of negative charge because it is connected to two Zn atoms. In the half-sandwich structure of the cationic compound **II**, however, considerable amounts of positive charge are found in the formally neutral PN ligand. Nevertheless, the results suggest that the internal charge separation between Zn and the cyclopentadienyl ligand is only to a small degree dependent on the hapticity, the molecular charge, the type of ring system, or the number of bonded rings.

Aspherical stockholder fragments: Inspection of the electron density distribution on a surface that reliably defines the outer contour of a molecular fragment within a molecule (e.g., a functional group) enables an estimation of the atom–atom connectivity that is in accordance with chemical sense. The advantage is that these distributions are not dependent on the existence of a bond path or virial path. Moreover, they neither refer to a single reference point, like the SF, nor do they display the electron sharing between a single pair of atoms, like the delocalization index, but provide insight into the interaction between two molecular fragments that may include large numbers of atoms. In that, these surfaces allow both a qualitative and quantitative interpretation of chemical bonding. The ASF surfaces applied here are closely related to the Hirshfeld surfaces, which are widely applied to analyze intermolecular interactions, see ref [46] and references therein for an overview and recent develop-

ments. Herein we use aspherical atomic densities, which we believe to be more meaningful for the interpretation of intramolecular contacts, instead of spherically averaged atomic densities. Figure 6 displays the electron density mapped onto the ASF surface for the Zn atom in the models **I**_{opt} (view from terminal Cp* ring; a), **I**_{opt} (central Cp* ring; b), **II**_{exp} (c), and **II**_{opt} (d). All surfaces are given in the same color scale to guarantee comparability. The number of Zn–C interactions represented by white lines corresponds to the number of V_2 –(Zn,C) basins, see next section. For the terminal η^5 -connected ring (a) a ring-shaped charge accumulation is visible with a maximum value ($0.401 \text{ e } \text{\AA}^{-3}$) considerably smaller than for the disc-shaped charge accumulation at the central $\eta^1(\pi)$ -connected ring in (b) ($0.519 \text{ e } \text{\AA}^{-3}$). Both for experimental and optimized geometries of compound **II**, the electron density shows a kidney-shaped distribution, which is symmetrical for the latter. Although being asymmetric for the experimental geometry, we conclude that the ring is η^2 bonded as well. The maxima of the ED are $0.480 \text{ e } \text{\AA}^{-3}$ for **II**_{exp} and $0.465 \text{ e } \text{\AA}^{-3}$ for **II**_{opt}.

Figure 7 displays the electron density mapped onto the ASF surface for models **III**_{exp} (Cp*) (a), **III**_{exp} (Cp*^N) (b), **IV**_{exp} (c), and **V**_{exp} (d). Apparently, all Zn–C contacts in Figure 7 have a disc-like shape with pronounced electron density accumulations (0.588 , 0.446 , 0.600 , and $0.599 \text{ e } \text{\AA}^{-3}$). Although for models **III**_{exp} (Cp*^N) and **IV**_{exp} weak triangular distortions of the ED are visible on the ASF surfaces, the ED distributions at the central regions around the Zn–C axes are clearly disc-shaped. Thus, η^3 type of bonding can be discarded for the Zn–C interactions of these two models. The ASF analysis confirms the virial-path analysis, see above.

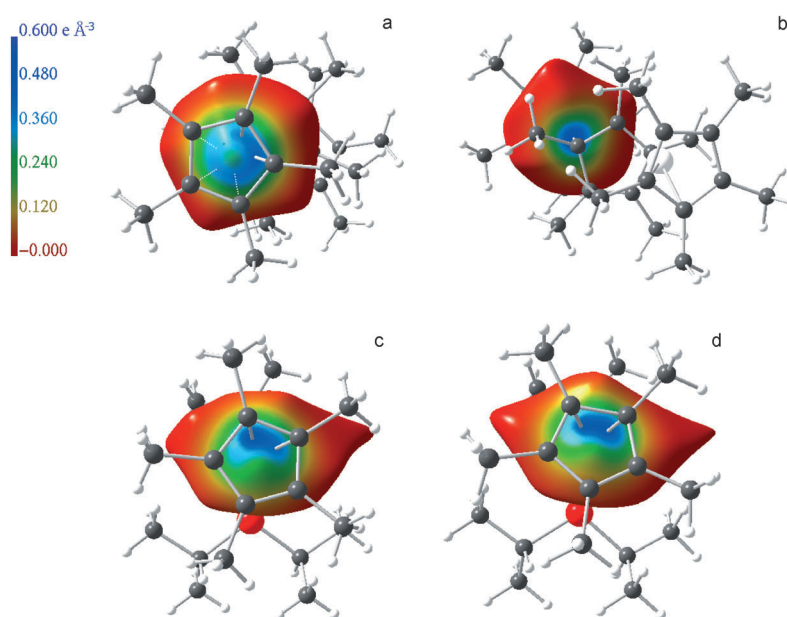


Figure 6. Electron density mapped onto the ASF surfaces of the Zn atoms in models **I**_{opt} view from terminal Cp* ring (a), **I**_{opt} view from central Cp* ring (b), **II**_{exp} (c), and **II**_{opt} (d). The color code is scaled for comparability.

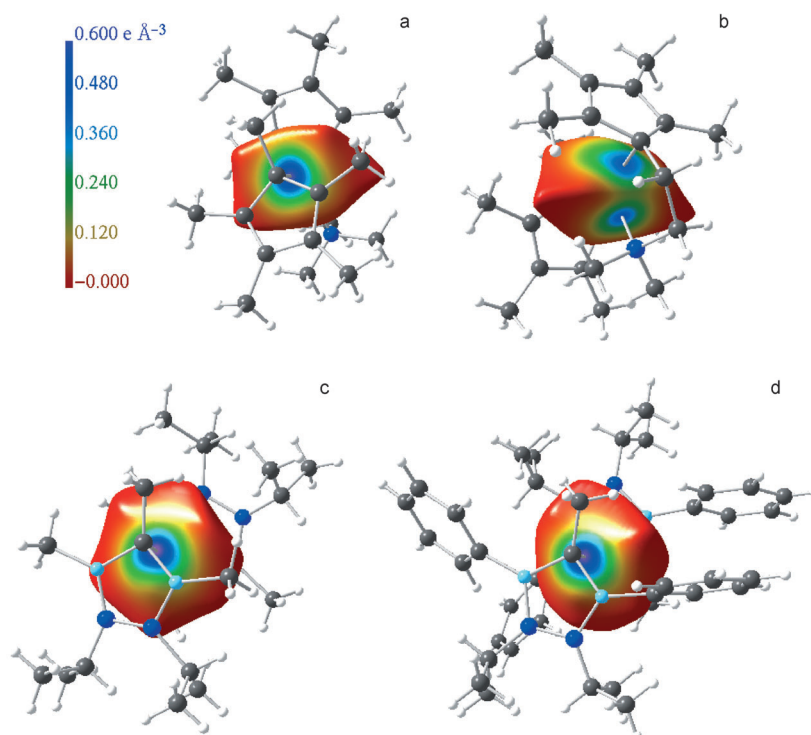


Figure 7. Electron density mapped onto the ASF surfaces of the Zn atoms in models **III**_{exp} Cp* (a), **III**_{exp} Cp*^N (b), **IV**_{exp} (c), and **V**_{exp} (d). The color code is scaled for comparability.

Figure 8 displays the electron density mapped onto the ASF surface of the terminal and central Cp* rings in model **I**_{opt} and a magnification of the corresponding bonding regions, together with the bonding region of model **II**_{exp}. For the terminal Cp* ring (a) a cone-shaped imprint is visible that, together with the ring-shaped electron accumulation, is

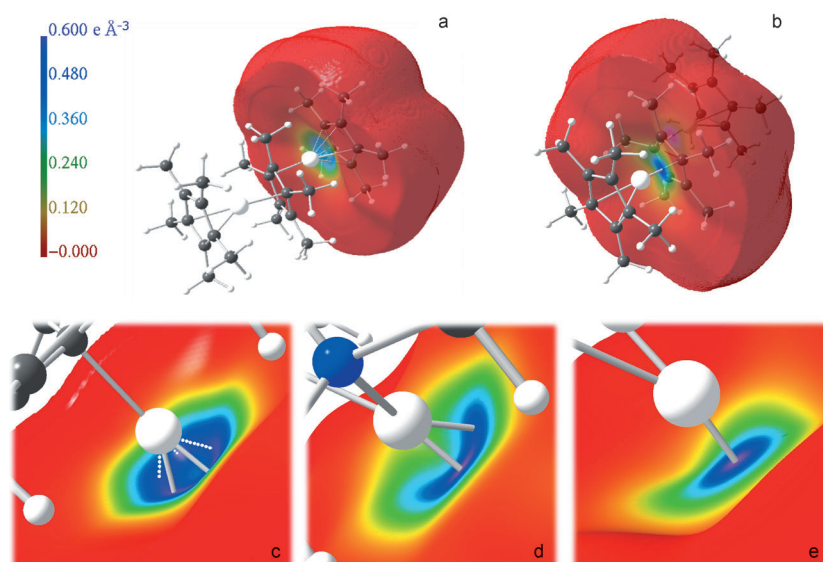


Figure 8. Electron density mapped onto the ASF surfaces of the Cp* rings in model \mathbf{I}_{opt} . a) terminal Cp* ring, b) central Cp* ring. The color code is scaled for comparability. c–e) Magnifications of the bonding regions for models \mathbf{I}_{opt} (terminal), \mathbf{II}_{exp} , and \mathbf{I}_{opt} (central). Color code is not scaled to highlight also small ED distribution effects.

characteristic for η^5 bonding (see Figure 8c). η^1 bonding on the other hand leads to a flat Zn–C surface close to the Zn–C axis, see Figure 8b and e. For intermediate bonding (η^2 in model \mathbf{II}_{exp}) the curvature of the ASF surface is in-between η^5 and η^1 (d) and the imprint is kidney-shaped. The curvature of the ASF surface is a surprisingly meaningful tool for

chemical interpretation and its calculation is aspired for further development of the ASF concept.

ELI-D analysis: It is known from an ELF study on the highly symmetric compounds ferrocene and bis-(benzene)chromium that the metal–Cp interactions lead to the generation of a new type of disynaptic valence basins, $V_2(\text{M},\text{C})$, M = metal atom, which in good approximation corresponds to M–C σ bonding.^[33] In the low-symmetry compounds investigated herein these types of basins are also found and the formation can directly be related to the hapticity. Moreover, the formerly disynaptic C–C valence basins within the free Cp* ring

become trisynaptic as they are connected to the metal atoms core basins after complex formation, $V_3(\text{M},\text{C},\text{C})$. They represent the π -bonding part of the M–C interaction. Figures 9, 10, 11, and 12 display the ELI-D at an isovalue of $Y=1.30$ for the models \mathbf{I}_{opt} , \mathbf{II}_{exp} , \mathbf{II}_{opt} , $\mathbf{III}_{\text{exp}}$, $\mathbf{III}_{\text{opt}}$, and \mathbf{IV}_{exp} . Due to the size of the compounds, the graphical representation is

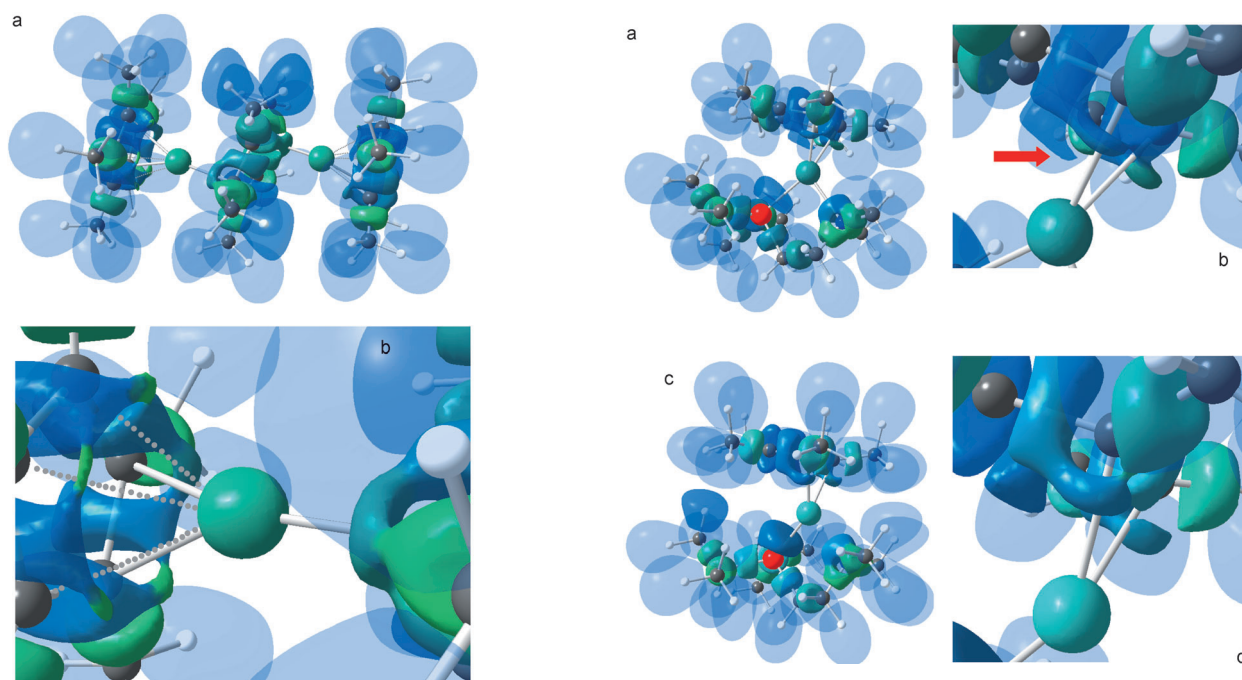


Figure 9. ELI-D representation of model \mathbf{I}_{opt} at an isovalue of $Y=1.30$. a) Complete molecule; b) magnification of the bonding region around one Zn atom.

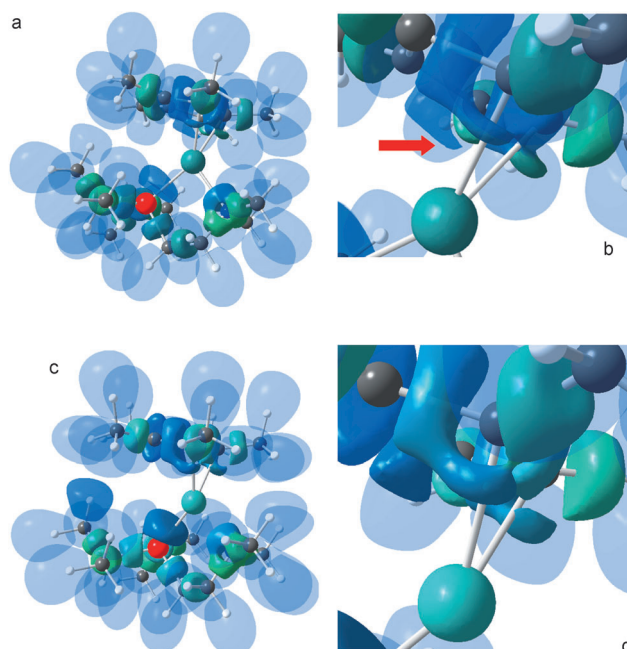


Figure 10. ELI-D representation of models \mathbf{II}_{exp} and \mathbf{II}_{opt} at an isovalue of $Y=1.30$. a,c) Complete molecules; b,d) magnification of the bonding region around the Zn atom. The red arrow indicates the incipient formation of a new $V_2(\text{Zn},\text{C})$ basin.

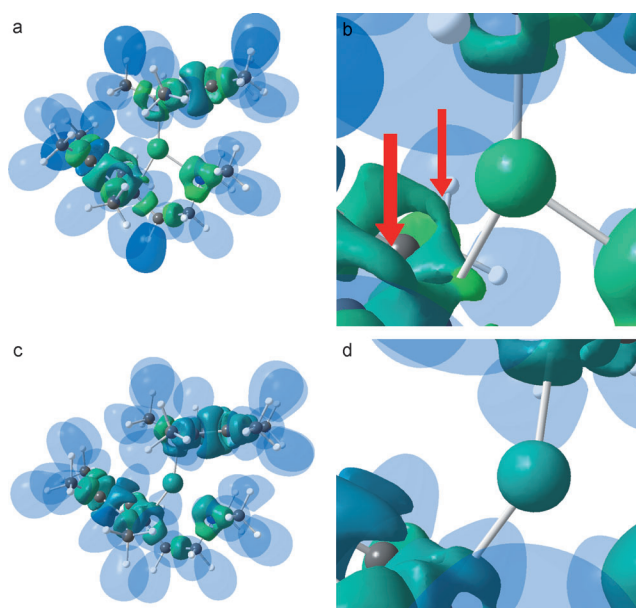


Figure 11. ELI-D representation of models **III**_{exp} and **III**_{opt} at an isovalue of $Y=1.30$. a,c) Complete molecules; b,d) magnification of the bonding region around the Zn atom. The red arrows indicate the incipient formation of two new $V_2(\text{Zn,C})$ basins.

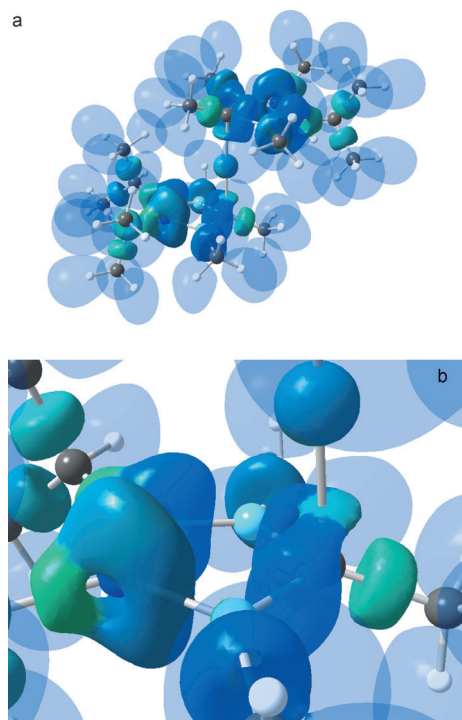


Figure 12. ELI-D representation of model **IV**_{exp} at an isovalue of $Y=1.30$. a) Complete molecule; b) magnification of the bonding region around the Zn atom.

complicated. To make it clearer, the monosynaptic protonated valence basins ($V_1(\text{C,H})$ or H atoms) are given in transparent mode. Moreover, the remaining localization domains

are color coded in the numerical order of increasing volume of the corresponding basins.

As expected, the $\eta^5 \text{Zn-Cp}^*_{\text{ter}}$ interaction in model **I**_{opt} leads to the generation of five $V_2(\text{Zn,C})$ basins, each carrying 0.41 e at an average, see Figure 9 and Table 4. The electron populations that constitute the newly formed $V_2(\text{Zn,C})$ basins almost exclusively descend from the C–C bonds within the aromatic Cp^* ring (now $V_3(\text{Zn,C,C})$). Accordingly, the latter carry an averaged population of 2.67 e, which is 0.37 e smaller than the value in the optimized gas-phase structure of the Cp^* anion ($N_{001} V_2(\text{C}_r, \text{C}_r) = 3.04 \text{ e}$). The C–Me bonds of the Cp^* ring are only slightly affected by the complex formation. The $\eta^1(\pi) \text{Zn-Cp}^*_{\text{cen}}$ interaction is characterized by one $V_2(\text{Zn,C})$ basin, which contains 1.21 e.

For model **II**_{exp}, two $V_2(\text{Zn,C})$ basins (0.72 e for $V(\text{Zn,C1})$, 0.65 e for $V(\text{Zn,C2})$) are found; this confirms the ASF surfaces analysis. However, close inspection of the Zn–C contacts (Figure 10b) reveals that the structure is quite close to a catastrophe scenario in which a third basin, $V_2(\text{Zn,C2}')$, may be generated, see red arrow. The topological instability of the electron distribution also explains the “missing” virial path as discussed in the previous section. After geometry optimization of compound **II** the structure unambiguously exhibits a symmetrical η^2 bonding mode with two $V_2(\text{Zn,C})$ basins, each containing 0.95 e, see Figure 10c,d.

For compound **III** both rings (Cp^* and Cp^{*N}) show only one Zn–C virial path (see Figure 4d) both in experiment and theory and the charge accumulation on the ASF surface shows a disc-like shape along the Zn–C axes in all cases (see Figure 7a,b). Accordingly, only one $V_2(\text{Zn,C})$ basin is found each for the Zn– Cp^* and the Zn– Cp^{*N} interaction, see Figure 11. Because the Cp^* ring represents $\eta^1(\sigma)$ type of bonding, it is not surprising that large electron populations of 1.84 e (exp) and 1.90 e (opt) are located within the $V_2(\text{Zn,C})$ σ basin. The Zn– Cp^{*N} interaction shows the remarkably small electron population of 0.49 e for the $V_2(\text{Zn,C})$ σ basin of the experimental geometry. Again, close inspection of the Zn–C contacts reveals that this structure is very close to a catastrophe scenario, because two pairs of neighboring $V_3(\text{Zn,C,C})$ domains are fused together at this isovalue, almost generating a set of two further $V_2(\text{Zn,C})$ σ basins, see red arrows in Figure 11b. As for compound **II**, these additional features disappear after geometry optimization, the $V_3(\text{Zn,C,C})$ basins are separated from each other and the $V_2(\text{Zn,C})$ σ basin is populated with 1.20 e (see Figure 11c,d), which compares well to the $\eta^1(\pi)$ -type Zn– $\text{Cp}^*(\text{cen})$ interaction in model **I**_{opt}.^[47]

Finally, also for compounds **IV**_{exp} (Figure 12) and **V**_{exp} (see the Supporting Information) the ELI-D supports the virial paths and ASF surfaces analyses in that only one $V_2(\text{Zn,C})$ σ basin is found for each ring, which carries 0.76 e (**IV**_{exp}) and 0.94 e (**V**_{exp}), respectively.

The results support the statement that η^3 -type bonding is not realized and that the molecular geometries that suggest η^3 bonding are most probably a consequence of the packing process within the crystal. In agreement with the virial-paths

Table 4. Topological and integrated ELI-D bond descriptors of free Cp*[−] and compounds **I** and **II**.^[a]

Model	Basin	No.	V_{001} [Å ³]	N_{001} [e]	μ_{\max}	Δ_{\max} [Å]	$N_{Zn}(\%)$ [e]	ΣN_{Zn} [e]
free Cp* [−]	$V_2(C_r, C_r)^{[b]}$	5	9.9	3.04	1.78	0.072	–	–
	$V_2(C_r, C_{Me})$	5	3.0	1.96	1.91	0.007	–	–
I _{opt} (ter)	$V_2(Zn, C)$	5	3.2	0.41	1.32	0.370	0.12(30.2)	0.62
	$V_3(Zn, C, C)$	5	6.5	2.67	1.82	0.116	0.06(2.1)	0.28
	$V_2(C_r, C_{Me})$	5	3.2	2.01	1.95	0.013	–	–
I _{opt} (cen)	$V_2(Zn, C)$	1	5.2	1.21	1.45	0.102	0.37(30.3)	0.37
	$V_3(Zn, C1^{(o)}, C2)$	2	5.6	2.59	1.84	0.116	0.05(2.0)	
	$V_3(Zn, C1^{(o)}, C3^{(o)})$	2	4.3	2.27	1.86	0.077	0.02(1.1)	
	$V_3(Zn, C3, C3')$	1	11.4	3.38	1.78	0.059	0.01(0.4)	0.17
	$V_2(C_r, C_{Me})$	5	3.2	1.99	1.95	0.009	–	–
II _{exp}	$V_2(Zn, C1)$	1	3.5	0.72	1.35	0.318	0.20(27.8)	
	$V_2(Zn, C2)$	1	5.0	0.65	1.34	0.385	0.20(30.8)	0.40
	$V_3(Zn, C1, C2)$	1	5.0	2.47	1.84	0.131	0.04(2.0)	
	$V_3(Zn, C1, C2')$	1	5.4	2.53	1.83	0.121	0.05(2.0)	
	$V_3(Zn, C2, C3)$	1	5.9	2.69	1.83	0.090	0.04(1.5)	
	$V_3(Zn, C2', C3')$	1	9.3	3.11	1.80	0.077	0.02(0.6)	
	$V_3(Zn, C3, C3')$	1	9.3	3.19	1.82	0.086	0.13(4.1)	0.27
	$V_2(C_r, C_{Me})$	5	3.0	1.90	1.93	0.011	–	–
	$V_2(Zn, N)$	1	5.0	2.22	1.82	0.029	0.11(5.0)	–
	$V_2(Zn, P)$	1	14.6	2.38	1.87	0.282	0.60(25.2)	–
II _{opt}	$V_2(Zn, C)$	2	6.1	0.95	1.39	0.345	0.30(31.4)	0.60
	$V_3(Zn, C1, C1')$	1	4.4	2.26	1.85	0.124	0.03(1.3)	
	$V_3(Zn, C1^{(o)}, C2^{(o)})$	2	5.7	2.56	1.83	0.096	0.03(1.2)	
	$V_3(Zn, C2^{(o)}, C3)$	2	9.2	2.99	1.81	0.065	0.01(0.3)	0.11
	$V_2(C_r, C_{Me})$	5	3.2	1.99	1.95	0.014	–	–
	$V_2(Zn, N)$	1	5.0	2.20	1.82	0.026	0.10(4.4)	–
	$V_2(Zn, P)$	1	14.6	2.39	1.89	0.295	0.61(25.5)	–

[a] For all basins: V_{001} is the basin volume cut at 0.001 a.u., N_{001} is the corresponding electron population, Y_{\max} is the value of the attractor, Δ_{\max} is the distance of the attractor to the atom–atom axis, $N_{Zn}(\%)$ is the absolute (relative) electron population of the basin within the AIM Zn atom, ΣN_{Zn} is the combined population within the AIM Zn atom of all basins of the same type. [b] $C_r = C$ atoms of the Cp* ring.

analysis, ELI-D basins are exclusively formed for Zn–X contacts shorter than 2.28 Å.

The topological analysis of the ELI-D shows that with increasing hapticity the $V_2(Zn, C)$ electrons are less localized; this is reflected in lower ELI-D values at the attractor position (Y_{\max}) and concomitantly larger distances of the attractor to the Zn–C axes: $Y_{\max} = 1.53$ for $\eta^1(\sigma)$, 1.45 for $\eta^1(\pi)$, 1.39 for η^2 , and 1.32 for η^5 . Figure 13 shows ELI-D attractors for the η^5 and $\eta^1(\pi)$ interactions of model **I**_{opt}. The former shows considerable shifts of the attractor positions outwards the conus, which is formed by the five Zn–C_r axes, see Δ_{\max} (distance of the attractor to the atom–atom axis) values in Table 4. This leads to a convex curvature of the Zn–attr–C bend and is in contrast to the corresponding virial paths, which are slightly concave close to the C atoms. This type of discrepancy between ED and ELI-D was formerly discovered for epoxides,^[48] which show S-shaped C–O bond paths (inwardly curved from C atoms to bcp), but C–O

ELI-D attractors outside the C–O–C triangle. In this respect, one has to remember that electron density and electron localization are not necessarily coincident. The electronic influence of the Zn atom on the $V_3(Zn, C, C)$ basins is visible in increasing Δ_{\max} values with decreasing Zn–C distance. The electrons within the $V_2(Zn, C)$ σ basins are less localized ($Y_{\max} = 1.32$ – 1.53) than the electrons within the $V_3(Zn, C, C)$ π basins ($Y_{\max} = 1.78$ – 1.87), see Tables 4 and 5. Thus, the latter come close to the value for the certainly quite localized $V_2(C_r, C_{Me})$ electrons ($Y_{\max} = 1.94$ – 1.95).

For all models, the $V_3(Zn, C, C)$ basin populations within the cyclic ligands vary according to the bond lengths alternation scheme given in Figure 3, see also Tables 4 and 5. For the CB₂N₂-rings, the situation is more complex, as three different bond types (one weak homopolar N–N bond, two dative N–B bonds, and two polar covalent B–C bonds) occur within these heterocycles; this is manifested in quite different electronic bond properties. With reference to the optimized gas-phase structures of the free CB₂N₂ rings, however, one also detects the expected

“bond alternation” with weaker C–B and stronger B–N bonds in the Zn complexes.

The sum of the electron populations of the Zn core basins, C(Zn), is 27.7–27.9 e for all models. This corresponds to the $(1s)^2(2s, p)^8(3s, p)^8(3d)^{10}$ electron configuration, which is expected for a Zn^{II} oxidation state. Because the 3d shell of the Zn atom is filled, the typical electron redistributions according to a “key–lock” arrangement between metal and ligand (generally visible in static deformation densities, the Laplacian of the density and localization functions, see for example ref. [49]) does not occur for zinocenes and related compounds. Nevertheless, a distortion of the complete Zn core basin shape (not a localization domain representation; here, zero-flux surfaces of the ELI-D are shown) is visible accompanied by a gradient in the electron localizability, which mirrors the degree of electron delocalization between Zn atom and ring systems. Figure 14 displays the ELI-D mapped on the surfaces of the C(Zn) basins for models **I**_{opt},

Table 5. Topological and integrated ELI-D bond descriptors of compounds **III** to **V**.^[a]

Model	Basin	No.	V_{001} [Å ³]	N_{001} [e]	μ_{\max}	Δ_{\max} [Å]	$N_{Zn}(\%)$ [e]	ΣN_{Zn} [e]
III_{exp} (Cp*)	$V_2(\text{Zn}, \text{C})$	1	9.5	1.84	1.53	0.111	0.69(37.5)	0.69
	$V_2(\text{Zn}, \text{N})$	1	5.1	2.19	1.82	0.097	0.09(4.3)	–
III_{opt} (Cp*)	$V_2(\text{Zn}, \text{C})$	1	12.3	1.90	1.52	0.107	0.79(41.9)	0.79
	$V_3(\text{Zn}, \text{C1}, \text{C2}^{(o)})$	2	3.8	2.20	1.87	0.073	0.01(0.3)	0.02
	$V_3(\text{Zn}, \text{C2}^{(o)}, \text{C3}^{(o)})$	2	11.9	3.39	1.78	0.069	–	–
	$V_3(\text{Zn}, \text{C3}, \text{C3}')$	1	5.2	2.47	1.86	0.067	–	–
	$V_2(\text{C}_T, \text{C}_{Me})$	5	3.2	2.00	1.95	0.007	–	–
III_{opt} (Cp*)	$V_2(\text{Zn}, \text{C})$	1	4.5	1.20	1.45	0.137	0.32(27.3)	0.32
	$V_3(\text{Zn}, \text{C1}, \text{C2}^{(o)})$	2	4.7	2.35	1.84	0.099	0.02(1.0)	–
	$V_3(\text{Zn}, \text{C2}^{(o)}, \text{C3}^{(o)})$	2	11.7	3.33	1.79	0.068	0.03(0.9)	0.11
	$V_3(\text{Zn}, \text{C3}, \text{C3}')$	1	6.6	2.67	1.83	0.062	–	–
	$V_2(\text{C}_T, \text{C}_{Me})$	5	3.1	1.98	1.94	0.010	–	–
III_{opt}	$V_2(\text{Zn}, \text{N})$	1	5.1	2.19	1.82	0.097	0.09(4.3)	–
IV_{exp}	$V_2(\text{Zn}, \text{C})$	1	3.6	0.76	1.38	0.153	0.26(34.2)	0.26
	$V_3(\text{Zn}, \text{C}, \text{B})$	2	9.7	2.70	1.91	0.143	0.23(8.5)	0.46
	$V_3(\text{Zn}, \text{B}, \text{N})$	2	6.5	3.04	1.76	0.152	–	–
	$V_3(\text{Zn}, \text{N}, \text{N})$	1	0.9	1.24	1.59	0.049	–	–
	$V_1(N_{Zn})$	1	4.5	1.31	1.64	–	–	–
	$V_1(\text{N})$	1	4.8	1.25	1.66	–	–	–
	$V_2(\text{C}_T, \text{C}_{Me})$	1	2.4	1.74	1.88	0.008	–	–
	$V_2(\text{B}_T, \text{C}_{Me})$	2	5.1	1.96	2.04	0.021	–	–
	$V_2(\text{N}_T, \text{C}_{iPr})$	2	1.9	1.66	1.77	0.040	–	–
	$V_2(\text{C}_T, \text{C}_{Me})$	1	2.4	1.73	1.88	0.010	–	–
V_{exp}	$V_2(\text{Zn}, \text{C})$	1	4.4	0.94	1.39	0.080	0.33(35.1)	0.35
	$V_3(\text{Zn}, \text{C}, \text{B})$	2	9.4	2.62	1.91	0.135	0.22(8.4)	0.44
	$V_3(\text{Zn}, \text{B}, \text{N})$	2	6.1	2.95	1.77	0.164	–	–
	$V_3(\text{Zn}, \text{N}, \text{N})$	1	1.0	1.27	1.60	0.044	–	–
	$V_1(N_{Zn})$	1	4.9	1.27	1.66	–	–	–
	$V_1(\text{N})$	1	5.5	1.41	1.67	–	–	–
	$V_2(\text{C}_T, \text{C}_{Me})$	1	2.4	1.73	1.88	0.010	–	–
	$V_2(\text{B}_T, \text{C}_{Ph})$	2	6.5	2.34	2.13	0.049	–	–
	$V_2(\text{N}_T, \text{C}_{iPr})$	2	1.8	1.69	1.76	0.033	–	–
	$V_2(\text{C}_T, \text{C}_{Me})$	1	2.4	1.73	1.88	0.010	–	–

[a] For all basins: V_{001} is the basin volume cut at 0.001 a.u., N_{001} is the corresponding electron population, μ_{\max} is the value of the attractor, Δ_{\max} is the distance of the attractor to the atom–atom axis, $N_{Zn}(\%)$ is the absolute (relative) electron population of the basin within the AIM Zn atom, ΣN_{Zn} is the combined population within the AIM Zn atom of all basins of the same type. For clarity, the $V_3(\text{Zn}, \text{C}, \text{C})$ basins of model **III_{exp}** are omitted.

II_{exp}, **III_{exp}**, and **IV_{exp}**. For the η^5 bonding mode one finds a conus-like distortion of the C(Zn) basin, which points towards the centroid of the Cp* ring (Figure 14a). For any type of η^1 bonding, ($\eta^1(\pi)$ or $\eta^1(\sigma)$), the C(Zn) basin surface approximates the shape of a sphere along the Zn–C axis and shows slightly higher localizability at this region. Intermediate hapticities are characterized by increased surface convexity and a horseshoe-shaped zone of decreased ELI-D values. Finally, for the dative Zn–N bonds, a pronounced flattening of the surface is detected accompanied by a de-

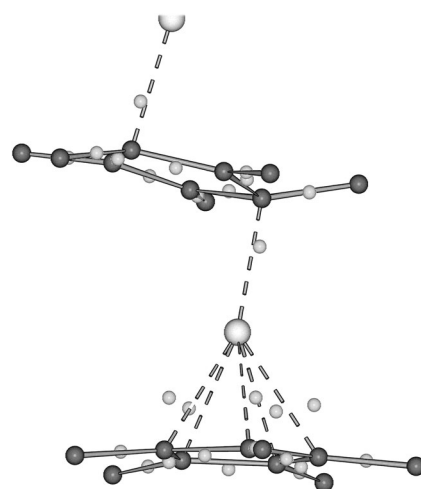


Figure 13. ELI-D attractor positions in model **I_{opt}**. Attractors given as light grey spheres.

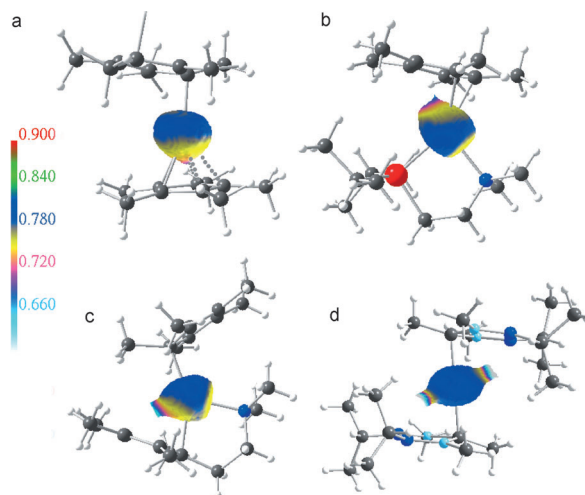


Figure 14. ELI-D representation of the C(Zn) basins. The ELI-D is mapped on the basins surfaces. a) Model **I_{opt}**, b) **II_{exp}**, c) **III_{exp}**, and d) **IV_{exp}**.

crease of localizability. For the less polarized Zn–P bond on the other hand, the spherical shape of the C(Zn) basin is preserved.

The different bonding modes η^5 – $\eta^1(\sigma)$ lead to different amounts of electrons transferred from the ligand to the metal atom. In terms of AIM charges, these differences turned out to be weak. Nevertheless, it is interesting to know in detail how the electron donation occurs. This is possible by the combined use of AIM and ELI-D space partitioning. The concept of overlapping ELI-D valence basins with AIM atoms was developed by Jansen and co-workers^[50] and used for the estimation of bond polarities (Jansen index= J). For homopolar bonds, for example, the C–C bond in ethane, the electrons within the $V_2(\text{C}, \text{C})$ bonding basin are to 50% located within each C atom, thus $J=50\%$. With increasing bond polarity, one finds an increasing amount of electron populations located within the more

electronegative atom ($J > 50\%$). Moreover, this concept helps to discriminate polar covalent interactions ($50\% < J < 95\%$) from dative bonds ($J > 95\%$) and allows a reliable estimation of the charge transfer between Lewis base and Lewis acid.^[51]

By comparing the absolute and relative electron populations of the $V_2(\text{Zn,C})$ σ basins and the $V_3(\text{Zn,C,C})$ π basins within the Zn AIM atoms ($N_{\text{Zn}}(\%)$, see Tables 4 and 5) the dominant metal–C π interaction proposed by Frison and Sevin for ferrocene and bis(benzene)chromium becomes questionable for Zn complexes. According to our results, all $V_2(\text{Zn,C})$ σ basins supply approximately 30% of the electrons to the Zn atom. This corresponds to absolute values of 0.32–0.79 e, added up according to the number of $V_2(\text{Zn,C})$ basins, see $\Sigma N_{(\text{Zn})}$ -values in Tables 4 and 5) and a polar covalent σ -bonding character ($\%(N_{\text{C}} \equiv J; J \text{ ca. } 70\%)$). The $V_3(\text{Zn,C,C})$ π basins, however, supply much smaller electron populations to the Zn atom (0.06 e for η^5 to almost zero for lower hapticities); this corresponds to $\Sigma N_{(\text{Zn})}$ values of 0.02–0.28 e and a dative π -bonding character, because the Jansen index is significantly above 95%. An exception are the $V_3(\text{Zn,C,B})$ basins in models **IV**_{exp} and **V**_{exp}, which donate 0.22 e each (0.44 e in total). This explains the lower AIM charges of the Zn atoms for the two compounds incorporating the diazadiborolyl ligand. Because we think that a significant Zn–C π interaction can only be assumed if the C=C bonding basin overlaps with the Zn AIM atom, we suggest to define the σ -to- π relation in the Zn–ring interaction as the relation of their respective electron donations to the AIM Zn atom as presented above. This leads to the following relative σ contributions: η^5 (**I**_{opt}): 68.9%, $\eta^1(\pi)$ (**I**_{opt}): 68.5%, $\eta^3?$ (**II**_{exp}): 59.7%, η^2 (**II**_{opt}): 84.5%, $\eta^1(\sigma)$ (**III**_{opt}, Cp*): 97.5%, $\eta^1(\pi)$ (**III**_{opt}, Cp*^N): 74.4%, $\eta^1(\pi)$ (**V**_{exp}): 44.3%.

Apparently, for all Cp*-derived ring systems, σ bonding dominates over π bonding, but for the diazadiborolyl ligand higher π contributions are detected. As expected, the σ contributions for the Cp* derivatives increase in the order $\eta^5 < \eta^2 < \eta^1(\sigma)$ (69%, 85%, 98%), but $\eta^3(?)$ and $\eta^1(\pi)$ show large variations (60%–75%). This is due to the fact that the Zn atom has contact to all (five) C–C bonding basins if it is located inside the ring perimeter, but because this does not necessarily lead to the formation of more $V_2(\text{Zn,C})$ basins, the π contributions increase in relation to the dominant σ bonding.

Conclusion

The concept of hapticity is a useful and indispensable tool in the interpretation of metal-to-ligand connectivities in metal–organic complexes, including different types of (delocalized) ring systems as ligands. By definition, such a concept is yes/no-based and moreover, the borderline between “connected” and “not connected” is always arbitrary. For highly symmetric metallocenes and related compounds, the hapticity is nevertheless usually self-evident by inspection of the molec-

ular geometry. This is not the case for the less symmetric zinocene-related compounds analyzed herein. Analysis of real-space functions, such as the electron density, and functionals, such as the ELI-D, however, helps to establish trends that relate the concept of hapticity to physical properties and proves to be superior to the exclusive inspection of the molecular geometry.

An important conclusion of our work is that η^3 type of bonding is hardly ever realized for Zn–carbocycle interactions and most probably a consequence of the packing process within the crystalline surrounding. However, one has to be aware that experimental geometries obtained by single-crystal diffraction often suffer from disorder and that already minor distortions in the geometry may lead to significant changes in the ED and/or ELI-D distribution. This phenomenon is long-time known for the ED and obviously also relevant for the ELI-D and related concepts. Nevertheless, in the overall picture our results are self-consistent and the proposed borderline of 2.3 Å seems to be reliable not only for cyclopentadienyl rings, but also for the diazadiborolyl-derived heterocycles.

Because the number of $V_2(\text{Zn,C})$ σ basins is dependent on the hapticity, an interpretation scheme was developed, which allows the quantification of σ and π contributions to the Zn–ring interactions in accordance with the proposed hapticity through determination of the overlap of the $V_2(\text{Zn,C})$ σ basins and $V_3(\text{Zn,C,C})$ π basins with the AIM Zn atoms. For all Zn–ring connectivities (η^5 – $\eta^1(\sigma)$) in the Cp* rings (compounds **I**–**III**), the σ contributions dominate over the π contributions. The diazadiborolyl-derived heterocycles are characterized by a pronounced overlap of the $V_3(\text{Zn,C,B})$ basins; this leads to dominant π contributions.

Acknowledgements

R. Herrmann is acknowledged for X-ray data collection and processing of compound **III**. P. Finke is acknowledged for support with the Gaussian calculations. S. Grabowsky acknowledges the ARC (Australian Research Council) for financial support within the Discovery Project DP110105347.

- [1] a) T. J. Kealy, P. L. Pauson, *Nature* **1951**, 168, 1039–1040; b) S. A. Miller, J. A. Tebbboth, J. F. Tremaine, *J. Chem. Soc.* **1952**, 632–635.
- [2] N. J. Long, *Metallocenes: An Introduction to Sandwich Complexes*; Blackwell Science, Oxford, U.K., **1998**.
- [3] a) I. Resa, E. Carmona, E. Gutierrez-Puebla, A. Monge, *Science* **2004**, 305, 1136–1138; b) I. Resa, E. Álvarez, E. Carmona, *Z. Anorg. Allg. Chem.* **2007**, 633, 1827–1831; c) D. Schuchmann, U. Westphal, S. Schulz, U. Flörke, D. Bläser, R. Boese, *Angew. Chem.* **2009**, 121, 821–824; *Angew. Chem. Int. Ed.* **2009**, 48, 807–810; d) T. Bollermann, K. Freitag, C. Gemel, R. W. Seidel, M. von Hopffgarten, G. Frenking, R. A. Fischer, *Angew. Chem.* **2011**, 123, 798–802; *Angew. Chem. Int. Ed.* **2011**, 50, 772–776; e) P. H. M. Budzelaar, J. Boersma, G. J. M. van der Kerk, A. L. Spek, J. M. Duisenberg, *J. Organomet. Chem.* **1985**, 281, 123–130; f) R. Blom, J. Boersma, P. H. M. Budzelaar, B. Fischer, A. Haaland, H. V. Volden, J. Weidlein, *Acta. Chem. Scand. A* **1986**, 40, 113–120; g) A. Haaland, S. Samdal, N. V. Tverdova, G. V. Girichev, N. I. Giricheva, S. A. Shly-

- kov, O. G. Garkusha, R. V. Lokshin, *J. Organomet. Chem.* **2003**, *684*, 351–358.
- [4] Y. Yamaguchi, W. Ding, C. T. Sanderson, M. L. Borden, M. J. Morgan, C. Kutal, *Coord. Chem. Rev.* **2007**, *251*, 515–524.
- [5] a) H. Sinn, W. Kaminsky, H.-J. Vollmer, R. Woldt, *Angew. Chem.* **1980**, *92*, 396–402; *Angew. Chem. Int. Ed. Engl.* **1980**, *19*, 390–392; b) P. A. Deck, T. J. Marks, *J. Am. Chem. Soc.* **1995**, *117*, 6128–6129.
- [6] a) A. Lühl, H. P. Nayek, S. Blechert, P. W. Roesky, *Chem. Commun.* **2011**, *47*, 8280–8282; b) J. F. Hartwig, *Organotransition Metal Chemistry: From Bonding to Catalysis*, University Science Books, Sausalito, California, **2010**, pp. 700–717; c) M. R. Gagné, T. J. Marks, *J. Am. Chem. Soc.* **1989**, *111*, 4108–4109.
- [7] J. M. Lopez del Amo, G. Buntkowsky, H.-H. Limbach, I. Resa, R. Fernández, E. Carmona, *J. Phys. Chem. A* **2008**, *112*, 3557–3565.
- [8] a) P. Jutzi, N. Burford, *Chem. Rev.* **1999**, *99*, 969–990; b) P. Jutzi, G. Reumann, *J. Chem. Soc. Dalton Trans.* **2000**, 2237–2244.
- [9] A π -bonding interaction between zinc and a cyclopentadienyl ligand mainly involves the empty 4p orbitals of appropriate symmetry, rather than the completely filled 3d orbitals of zinc. The latter are too low in energy, which precludes a classical π -backbonding scenario as observed for transition metals with partially filled d orbitals. For a molecular orbital scheme of the ZnCp fragment see: E. S. J. Robles, A. M. Ellis, T. A. Miller, *J. Phys. Chem.* **1992**, *96*, 3247–3258. Note that π contributions have also been discussed for cadmium cyclopentadienyl complexes: C. C. Cummins, R. R. Schrock, W. M. Davis, *Organometallics* **1991**, *10*, 3781–3785.
- [10] D. A. Walker, T. J. Woodmann, M. Schormann, D. L. Hughes, M. Bochmann, *Organometallics* **2003**, *22*, 797–803.
- [11] B. Fischer, P. Wijkens, J. Boersma, G. van Koten, *J. Organomet. Chem.* **1989**, *376*, 223–233.
- [12] H. V. Ly, T. D. Forster, M. Parvez, R. McDonald, R. Roesler, *Organometallics* **2007**, *26*, 3516–3523.
- [13] H. Wang, G. Kehr, R. Fröhlich, G. Erker, *Angew. Chem.* **2007**, *119*, 4992–4995; *Angew. Chem. Int. Ed.* **2007**, *46*, 4905–4908.
- [14] M. A. Chilleck, T. Braun, B. Braun, *Chem. Eur. J.* **2011**, *17*, 12902–12905.
- [15] R. F. W. Bader, *Atoms in Molecules: A Quantum Theory*, Cambridge University Press, Oxford U.K., **1991**.
- [16] a) M. Kohout, *Int. J. Quantum Chem.* **2004**, *97*, 651–658; b) M. Kohout, F. R. Wagner, Y. Grin, *Theor. Chem. Acc.* **2008**, *119*, 413–420.
- [17] Unpublished results: Data for the X-ray structure analysis: $M = 392.91 \text{ g mol}^{-1}$; crystal dimensions: $0.40 \times 0.37 \times 0.19 \text{ mm}^3$; monoclinic, $P2_1/c$; $a = 8.8515(3)$, $b = 15.1751(4)$, $c = 16.2700(6) \text{ Å}$; $\beta = 99.733(3)^\circ$; $V = 2153.97(12) \text{ Å}^3$; $Z = 4$; $\rho_{\text{calc}} = 1.212 \text{ g cm}^{-3}$; $2\theta_{\text{max}} = 59.0^\circ$; $\lambda = 0.71073 \text{ Å}$ ($\text{MoK}\alpha$ radiation), $T = 100(2) \text{ K}$; STOE IPDS2T diffractometer; 40110 reflections collected, 5986 unique ($R_{\text{int}} = 7.83$), $4440 > 2\sigma$; $\mu = 1.145 \text{ mm}^{-1}$, face-indexed absorption correction, $T_{\text{min}} = 0.6721$, $T_{\text{max}} = 0.8412$; $R_1 = 4.40$, $wR_2(\text{ref}) = 12.77$; $\rho_{\text{min}} = -0.926 \text{ e Å}^{-3}$, $\rho_{\text{max}} = 0.624 \text{ e Å}^{-3}$. Selected bond lengths [Å] and angles [$^\circ$]: Zn–C1 ($\text{Cp}^{*\text{N}}$) 2.139(2), Zn–C2 ($\text{Cp}^{*\text{N}}$) 2.341(3), Zn–C2' ($\text{Cp}^{*\text{N}}$) 2.463(3), Zn–C1 (Cp^*) 2.017(2), Zn–N 2.142(2); N–Zn–C1 ($\text{Cp}^{*\text{N}}$) 84.89(9), N–Zn–C1 (Cp^*) 122.19(9), C1($\text{Cp}^{*\text{N}}$)–Zn–C1(Cp^*) 152.61(10). CCDC-867160 contains the supplementary crystallographic data for this paper. These data can be obtained free of charge from The Cambridge Crystallographic Data Centre via www.ccdc.cam.ac.uk/data_request/cif.
- [18] This was found before by Farrugia et al., see ref. [25].
- [19] One exception was detected for the virial paths, see Results and Discussion.
- [20] G. Frenking, N. Fröhlich, *Chem. Rev.* **2000**, *100*, 717–774.
- [21] M. Iwata, Y. Saito, *Acta Crystallogr. Sect. B* **1973**, *29*, 822–832.
- [22] a) T. Koritsánszky, P. Coppens, *Chem. Rev.* **2001**, *101*, 1583–1628; b) P. Macchi, A. Sironi, *Coord. Chem. Rev.* **2003**, *238–239*, 383–412; c) C. Gatti, *Z. Kristallogr.* **2005**, *220*, 399–457.
- [23] R. Ponec, C. Gatti, *Inorg. Chem.* **2009**, *48*, 11024–11031.
- [24] S. Mebs, R. Kalinowski, S. Grabowsky, D. Förster, R. Kickbusch, E. Justus, W. Morgenroth, C. Paulmann, P. Luger, D. Gabel, D. Lentz, *Inorg. Chem.* **2011**, *50*, 90–103.
- [25] L. J. Farrugia, C. Evans, D. Lentz, M. Roemer, *J. Am. Chem. Soc.* **2009**, *131*, 1251–1268.
- [26] R. F. W. Bader, C. Gatti, *Chem. Phys. Lett.* **1998**, *287*, 233–238.
- [27] C. Gatti, F. Cargnoni, L. Bertini, *J. Comp. Chem.* **2003**, *24*, 422–436.
- [28] R. F. W. Bader, M. E. Stephens, *J. Am. Chem. Soc.* **1975**, *97*, 7391–7399.
- [29] X. Fradera, M. A. Austen, R. F. W. Bader, *J. Phys. Chem. A* **1999**, *103*, 304–314.
- [30] a) A. D. Becke, K. E. Edgecombe, *J. Chem. Phys.* **1990**, *92*, 5397–5403; b) B. Silvi, A. Savin, *Nature* **1994**, *371*, 683–686.
- [31] a) M. Kohout, A. Savin, *Int. J. of Quantum Chem.* **1996**, *60*, 875–882; b) M. Kohout, F. R. Wagner, Y. Grin, *Int. J. of Quantum Chem.* **2006**, *106*, 1499–1507.
- [32] R. F. W. Bader, S. Johnson, T.-H. Tang, *J. Phys. Chem.* **1996**, *100*, 15398–15415.
- [33] G. Frison, A. Sevin, *Internet Electron. J. Mol. Des.* **2004**, *3*, 222–232.
- [34] a) F. L. Hirshfeld, *Theor. Chim. Acta* **1977**, *44*, 129–139; b) M. A. Spackman, P. G. Byrom, *Chem. Phys. Lett.* **1997**, *267*, 215–220.
- [35] a) T. Ziegler, *Chem. Rev.* **1991**, *91*, 651–667; b) A. Schäfer, C. Huber, R. J. Ahlrichs, *Chem. Phys.* **1994**, *100*, 5829–5835.
- [36] Gaussian 03, Revision E.01, M. J. Frisch, G. W. Trucks, H. B. Schlegel, G. E. Scuseria, M. A. Robb, J. R. Cheeseman, J. A. Montgomery, Jr., T. Vreven, K. N. Kudin, J. C. Burant, J. M. Millam, S. S. Iyengar, J. Tomasi, V. Barone, B. Mennucci, M. Cossi, G. Scalmani, N. Rega, G. A. Petersson, H. Nakatsuji, M. Hada, M. Ehara, K. Toyota, R. Fukuda, J. Hasegawa, M. Ishida, T. Nakajima, Y. Honda, O. Kitao, H. Nakai, M. Klene, X. Li, J. E. Knox, H. P. Hratchian, J. B. Cross, V. Bakken, C. Adamo, J. Jaramillo, R. Gomperts, R. E. Stratmann, O. Yazyev, A. J. Austin, R. Cammi, C. Pomelli, J. W. Ochterski, P. Y. Ayala, K. Morokuma, G. A. Voth, P. Salvador, J. J. Dannenberg, V. G. Zakrzewski, S. Dapprich, A. D. Daniels, M. C. Strain, O. Farkas, D. K. Malick, A. D. Rabuck, K. Raghavachari, J. B. Foresman, J. V. Ortiz, Q. Cui, A. G. Baboul, S. Clifford, J. Cioslowski, B. B. Stefanov, G. Liu, A. Liashenko, P. Piskorz, I. Komaromi, R. L. Martin, D. J. Fox, T. Keith, M. A. Al-Laham, C. Y. Peng, A. Nanayakkara, M. Challacombe, P. M. W. Gill, B. Johnson, W. Chen, M. W. Wong, C. Gonzalez, J. A. Pople, Gaussian, Inc., Wallingford CT, **2004**.
- [37] M. Kohout, DGrid, Version 4.5, Max-Planck-Institut für Chemische Physik fester Stoffe, Dresden, Germany, **2010**.
- [38] AIM2000—A Program to Analyse and Visualize Atoms in Molecules: F. Biegler-König, J. Schönbohm, D. Bayles, *J. Comput. Chem.* **2001**, *22*, 545–559.
- [39] T. A. Keith, AIMAll, Version 11.12.19, TK Gristmill Software, Overland Park KS, USA, **2011** (aim.tkgristmill.com).
- [40] D. Jayatilaka, D. J. Grimwood in *Computational Science—ICCS 2003, Part 4: Tonto: A Fortran Based Object-Oriented System for Quantum Chemistry and Crystallography*, Springer, New York, **2003**, pp. 142–151.
- [41] a) N. K. Hansen, P. Coppens, *Acta Crystallogr. Sect. A* **1978**, *34*, 909–921; b) A. Volkov, P. Macchi, L. J. Farrugia, C. Gatti, P. Mallinson, T. Richter, T. Koritsánszky, XD2006: A Computer Program for Multipole Refinement, Topological Analysis of Charge Densities and Evaluation of Intermolecular Energies from Experimental or Theoretical Structure Factors, User Manual, **2006**.
- [42] C. B. Hübschle, P. Luger, *J. Appl. Crystallogr.* **2006**, *39*, 901–904.
- [43] E. Keller, SCHAKAL: A Fortran Program for the Graphical Representation of Molecular and Solid-State Structure Models, Albert-Ludwigs-Universität Freiburg, Germany, **1999**.
- [44] The slippage of the Zn atom is defined as the distance between the ring centroid (Cg) and the perpendicular projection of the Zn atom to the ring plane.
- [45] C. Gatti, L. Bertini, *Acta Crystallogr. Sect. A* **2004**, *60*, 438–449.
- [46] M. A. Spackman, D. Jayatilaka, *Cryst. Eng. Comm.* **2009**, *11*, 19–32.
- [47] Although a grid step interval of 0.04 bohr is expected to provide reliable results concerning the basin separation, finer grids of 0.02 bohr step size were calculated for the Zn–Cp* interaction of model **II**_{exp} and the Zn–Cp^{*N} interaction of model **III**_{exp} to prevent

- misinterpretation of the data. This procedure, however, resulted in the same number of $V_2(\text{Zn,C})$ basins.
- [48] S. Grabowsky, D. Jayatilaka, S. Mebs, P. Luger, *Chem. Eur. J.* **2010**, *16*, 12818–12821.
- [49] S. Mebs, J. Henn, B. Dittrich, C. Paulmann, P. Luger, *J. Phys. Chem. A* **2009**, *113*, 8366–8378.
- [50] a) S. Raub, G. Jansen, *Theor. Chem. Acc.* **2001**, *106*, 223–232; b) I. Vidal, S. Melchor, J. A. Dobado, *J. Phys. Chem. A* **2005**, *109*, 7500–7508.
- [51] a) S. Mebs, S. Grabowsky, D. Förster, R. Kickbusch, M. Hartl, L. L. Daemen, W. Morgenroth, P. Luger, B. Paulus, D. Lentz, *J. Phys. Chem. A* **2010**, *114*, 10185–10196; b) S. Mebs, R. Kalinowski, S. Grabowsky, D. Förster, R. Kickbusch, E. Justus, W. Morgenroth, C. Paulmann, P. Luger, D. Gabel, D. Lentz, *J. Phys. Chem. A* **2011**, *115*, 1385–1395.

Received: March 15, 2012
Published online: August 14, 2012